

## Influence of Microstructure on the Corrosion Resistance of AISI 317L (UNS S31703)

Sérgio Souto Maior Tavares<sup>a\*</sup>, Gabriel Fracalossi Feijó<sup>a</sup>, Humberto Nogueira Farneze<sup>b</sup>,  
Maria José Ramos Sandim<sup>c</sup>, Isnaldi Rodrigues de Souza Filho<sup>c</sup>

<sup>a</sup> Departamento de Engenharia Mecânica, Universidade Federal Fluminense, CEP 24210-240, Niterói, RJ, Brazil

<sup>b</sup> Centro Federal de Educação Tecnológica-CEFET, Unidade Itaguaí - CEFET/RJ, CEP 23810-000, Itaguaí, RJ, Brazil

<sup>c</sup> Escola de Engenharia de Lorena, Universidade de São Paulo, CEP 12602-810, Lorena, SP, Brazil

Received: December 20, 2016; Revised: April 08, 2017; Accepted: April 21, 2017

The AISI 317L stainless steel is an austenitic grade with at least 3%Mo. Recently, this steel has replaced AISI 316L in many applications in chemical and petrochemical industries, due to its higher pitting corrosion resistance. The microstructure of the hot rolled and annealed material studied in this work consists of austenitic grains and 4.0% of delta ferrite ( $\delta$ ) with elongated islands morphology. This microstructure was modified by three processes: cold rolling with 87% of reduction, aging at 450°C for 400 h, and welding by gas tungsten arc welding (GTAW) process. The corrosion resistance was evaluated by anodic polarization tests (ASTM G-61) and critical pitting temperature tests (ASTM G-150). Cold rolling produced a microstructure consisting of elongated grains of austenite and martensite  $\alpha'$ , high dislocation density and the elongated islands of delta ferrite present in the annealed material. Welding produced a dendritic microstructure with 7.0% of delta ferrite and some  $\sigma$  precipitated in the ferrite. Finally, the aging at 450°C for 400 h provoked the decomposition of ferrite. The results show that these microstructural changes affected the pitting corrosion resistance, as detected by ASTM G-61 and ASTM G-150 tests.

**Keywords:** AISI 317L, austenitic stainless steel, pitting corrosion, critical pitting temperature

### 1. Introduction

Corrosion resistant alloys are frequently ranked by using the PREN (Pitting resistant equivalent number), as regard to the localized corrosion resistance, mainly pitting and crevice. The most accepted equations for PREN include the elements Cr, Mo and N<sup>1,2</sup>.

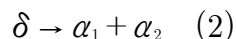
$$PREN = \%Cr + 3.3 \left( \frac{\%Mo + (0.5(\%Mo))}{16(\%N)} \right) \quad (1)$$

According to some authors, the multiplication factor of nitrogen in formulae (1) is 30 for austenitic steels<sup>1,3</sup>. The PREN has been used for austenitic, ferritic, supermartensitic and austenitic-ferritic stainless steels, and nickel alloys. Table 1 shows a comparison of chemical compositions (Cr, Mo, W, N) and PREN for austenitic 304L, 316L, 317L, lean duplex UNS S32304 and duplex UNS S31803 alloys.

The AISI 317L (UNS S31703) has a microstructure predominantly austenitic, with Mo contents in the range of 3 to 4%. According to the PREN, the pitting corrosion resistance of AISI 317L is superior to AISI 316L (austenitic) and UNS S32304 (austenitic-ferritic), but inferior to UNS S31803 and UNS S32205 (austenitic-ferritic).

Since Mo is a ferritizing element, the AISI 317L steel has a higher tendency to present delta ferrite ( $\delta$ ) in the microstructure. It appears as elongated islands in wrought products and as interdendritic phase in fusion welds. Furthermore, the high Mo content also increases the tendency to form intermetallic phases, such as sigma ( $\sigma$ ) and chi ( $\chi$ ).

Ferritic stainless steels and the ferrite phase of duplex and austenitic stainless steels are also susceptible to decomposition into a low Cr and a high Cr phases during aging in the range of 350°C to 550°C. The Cr-rich phase ( $\alpha_1$ ) forms by a mechanism of spinodal decomposition, which also produces nanometric regions depleted in Cr ( $\alpha_2$ )<sup>5-7</sup>. The reaction can be described as follows:



Fine  $\alpha_1$  precipitates can cause embrittlement and hardening of ferrite in long term aging<sup>6,9</sup>. The higher kinetics of reaction (2) occurs at 475°C and, for this reason, the expressions “475°C embrittlement” and “475°C hardening” have been used for ferritic and duplex steels exposed or treated around this temperature. Another consequence of long-term aging is the corrosion resistance decay due to the Cr-depleted regions in the matrix  $\alpha_2$ <sup>10-12</sup>.

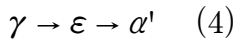
Cold deformation of austenitic stainless steels may transform austenite into martensite, depending on several

\* e-mail: ssmtavares@terra.com.br

**Table 1:** Cr, N, W and Mo contents specified and minimum PRE values for grades UNS S30403, S31603, S31703, S32304, S31803, and S32205 (%wt).<sup>4</sup>

UNS grade (AISI)	Cr	Mo	W	N	PREN (min.)
S30403 (304L)	18.0 – 20.0	--	-	--	19.0
S31603 (316L)	16.0 – 18.0	2.0 – 3.0	-	-	22.6
S31703 (317L)	18.0 – 20.0	3.0 – 4.0	-	-	27.9
S32304	21.0 – 23.0	0.05 – 0.60	-	0.05 – 0.20	22.0
S31803	21.0 – 23.0	2.5 – 3.5	-	0.08 – 0.20	30.5
S32205	22.0 – 23.0	3.0 – 3.5	-	0.14 – 0.20	34.1

metallurgical factors<sup>13</sup>. Among these factors, one can cite stacking fault energy (SFE), which is influenced by temperature and the chemical composition of the material<sup>14</sup>. In this context, two types of martensite may be formed upon deformation, following the reactions:



where  $\varepsilon$  is the hexagonal closed packed (hcp) martensite formed in the stacking faults produced by cold working, and  $\alpha'$  is the body centered cubic (bcc) martensite. It has been observed that  $\varepsilon$ -martensite is formed at low strains in some low-SFE metastable steels, such as AISI 304 and 316<sup>15-16</sup>. Generally, reaction (4) takes place for metastable austenitic steels with SFE < 20 mJ/m<sup>2</sup><sup>17</sup>. The amount of  $\varepsilon$  that can be formed in conventional austenitic stainless steels is also small, although it was believed that the only way to form  $\alpha'$ -martensite was through  $\varepsilon$  phase, as described by equations (3)<sup>16</sup>. However, lately it was proven that the direct transformation  $\gamma \rightarrow \alpha'$  is also possible by means of dislocation reactions<sup>18</sup>. By using Reed and Schramm empirical formula, a SFE of ~ 63 mJ/m<sup>2</sup> is found for the AISI 317L<sup>19</sup> steel. Therefore,  $\alpha'$ -martensite formation in this steel is expected to be ruled by reaction (5).

Many authors studied the deformation induced martensites in austenitic<sup>15-22</sup>, duplex and lean duplex stainless steels<sup>23-24</sup>. Both  $\varepsilon$ - and  $\alpha'$ - martensites can be observed by transmission electron microscopy (TEM) and quantified by X-ray diffraction (XRD). Additionally,  $\alpha'$ -martensite is ferromagnetic and, thus, can also be quantified by magnetic measurements<sup>20-24</sup>.

It is worth noting that the Cr-rich precipitate produced by spinodal decomposition and the magnetic martensite produced by cold working are usually cited with the same symbol ( $\alpha'$ )<sup>5-24</sup>, but these are phases completely distinct. For this reason, in this paper, the Cr-rich precipitate produced by spinodal decomposition was called  $\alpha_1$ .

The purpose of this work was to investigate the influence of some common fabrication operations and high temperature exposure on the microstructure and corrosion resistance of an AISI 317L stainless steel. As fabrication operations,

welding with gas tungsten arc welding (GTAW) process and cold deformation were investigated. Since the maximum temperature that facilities and accessories of AISI 317L are submitted is around 450°C, this temperature was chosen for thermal aging.

## 2. Experimental

The as-received (AR) AISI 317L steel was a 3-mm thick hot-rolled plate. For the GTAW welding, the AR material was used as the base metal. Table 2 shows the chemical composition of the base material and filler metal used in the GTAW process. The chemical composition of the filler metal is similar to the base material, except for the higher Ni content. PREN values calculated from equation (1) are also reported in Table 2. The weld was performed toward the perpendicular direction to the rolling direction following the parameters depicted in Table 3. A specimen of the weld metal, named WM, was cut for corrosion tests.

The as-received material was cold-rolled up to 87% of thickness reduction (or to a true deformation in thickness of 2.04) in several passes. In this work, the 87% cold-rolled steel was named as 87%-CR.

Another specimen, named A-450, was heat treated at 450°C for 400 h from the as received condition.

Microstructural characterization was performed by light optical microscopy (LOM), scanning electron microscopy (SEM), ferritoscope, and magnetic measurements in a vibrating sample magnetometer (VSM). Specimens with intermediary degrees of deformation till that of sample CR were produced and analyzed in the VSM, to evaluate the formation of magnetic martensite ( $\alpha'$ ). The maximum magnetic field applied (H) in the VSM was 16000 Oe, and the saturation magnetization ( $M_s$ ) was obtained with the extrapolation of the curve  $M \times 1/H$  for  $1/H=0$ , where M is the magnetization (emu/g).

Specimens WM, 87%-CR, A-450 and AR (as received) were used to prepare the working electrodes for electrochemical corrosion tests. Two corrosion tests were applied. Cyclic polarization tests in 3.5% NaCl solution were used to evaluate the pitting corrosion resistance, as detailed described in the ASTM G-61 standard<sup>25</sup>. A three electrodes cell, with working electrode of the material analyzed, reference and counter-

**Table 2:** Chemical compositions of weld metal and filler metal (Fe=bal.)

Sample	C	Mn	Si	S	P	Cr	Ni	Mo	PREN
Base metal	0.024	1.34	0.47	0,003	0.031	18.13	11.41	3.02	28.1
Filler metal	0.008	1.63	0.61	0,003	0.028	18.26	13.63	3.08	28.4

**Table 3:** Welding parameters and average welding energy.

$\phi$ (mm)	Polarity	Current (A)	Voltage (V)	ES (kJ/mm)	N° Passes
1.6	CC-	112-150	9-10	1.0	6

electrode were used. Working electrodes were prepared with the specimen to be analyzed embedded in epoxy resin among with a cooper wire for electric contact. Saturated calomel electrode was used as reference and a Pt wire was used as counter-electrode. The tests were conducted with the solution at 22 °C. After the stabilization of the open circuit potential ( $E_{ocp}$ ) the anodic polarization with sweep rate 1 mV/s initiated. The sweeping was reverted to the cathodic direction when the current density achieved 1mA/cm<sup>2</sup>.

The second corrosion test performed was the potentiostatic method to determine the cyclic polarization test, described in ASTM G-150<sup>26</sup>. The electrolyte was 1M NaCl solution. The working electrode is cathodically polarized with +700 mV. The heating rate of the solution was 1°C/minute. The CPT is defined in the ASTM G-150<sup>26</sup> as the temperature at which the current density achieves 100  $\mu$ A/cm<sup>2</sup> and remain above this value at least 60 s.

Each corrosion test was repeated three times per specimen.

### 3. Results and discussion

Figures 1(a-d) show important features of the microstructures of specimens AR, 87%-CR, WM and A-450. From Figure 1 (a), it is clear that the as-received specimen (AR) has a hot-rolled microstructure with recrystallized austenitic grains and elongated delta ferrite ( $\delta$ ) islands parallel to the RD. The amount of delta ferrite ( $\delta$ ) measured with ferritoscope was 4.0%. The 87%-CR specimen, in turn, has a typical cold rolled aspect. In Figure 1 (b), it is possible to see that austenitic grains were elongated and found among very fine  $\delta$  islands. The microstructure of specimen GTAW consists of austenite dendrites and interdendritic  $\delta$ , as shown in Figure 1 (c). For this specimen, the  $\delta$  content measured with ferritoscope was 7%, and is coherent with the prediction of WRC-92 diagram<sup>27</sup>. However, in some interdendritic regions it was observed intermetallic precipitates with high Cr and Mo contents, as shown in Figure 1(c). The microstructure of specimen A-450 shows the initial stage of ferrite decomposition into  $\alpha_1$  and  $\alpha_2$  (Figure1(d)).

The  $M_s$  versus true deformation ( $\epsilon$ ) behavior is shown in Figure 2. The  $M_s$  increases for  $\epsilon > 1.0$ , and reaches 6.10 emu/g in the specimen with  $\epsilon = 2.04$  ( $r=87\%$ ). Considering that the  $M_s$  increased from 2.75 emu/g in the AR sample to of 6.10 emu/g in the 87%-CR sample, the difference (3.35

emu/g) can be attributed to the  $\alpha'$  martensite formation. The quantification of  $\alpha'$  is possible if the magnetization saturation intrinsic of martensite ( $M_{s(i)}$ ) is known. This value is strongly dependent on the chemical composition of the steel. In the case of AISI 317L steel a rough estimative is to consider a value intermediary between those of AISI 304L (160.4 emu/g<sup>13</sup>) and duplex UNS S31803 (133.0 emu/g<sup>18</sup>). Thus, adopting  $M_{s(i)} = 146.8$  emu/g, the amount of  $\alpha'$  formed by cold deformation should be around 2.3%.

Table 4 shows the pitting ( $E_{pit}$ ) and repassivation ( $E_{rp}$ ) potentials measured in the cyclic polarization tests. Figure 3 shows the cyclic polarization curves representative of each condition. Some doubts arise when the measured breakdown or pitting potential is around 1.00  $V_{SCE}$ , because the abrupt increase of current density may be associated to oxygen evolution due to the hydrolysis of water, and, in this case, the value measured is not the pitting potential. This doubt can be clarified by the inspection of the surfaces after the tests. If pits are observed, the current density increase can be attributed to the pitting potential.

Specimen AR has a high pitting potential ( $E_{pit}$ ) and the curve does not show hysteresis, which means that its repassivation potential  $E_{rp}$  is closer to the  $E_{pit}$  (Figure3(a)). This behavior indicates a high pitting resistance in the test solution. In contrast, the curve of specimen 87%CR (Figure 3(b)) shows indications of metastable pits before the  $E_{pit}$  and the cyclic polarization curve presents a large hysteresis, with the  $E_{rp}$  value very low and closer to the open circuit potential ( $E_{ocp}$ ). This behavior indicates lower pitting resistance than the un-deformed steel, despite of the high  $E_{pit}$  value. Cold deformation produces a microstructure of crystalline defects and 2.3% of martensite, which may be the cause of the lower corrosion resistance when compared to the annealed material. The curve of specimen A-450 (Figure 3(c)) is similar to the 87%-CR, also presenting a large hysteresis, but without indications of metastable pits. Specimen WM is probably the less resistant to pitting corrosion, since its pitting potential ( $E_{pit}$ ) is significantly lower than in other specimens, and a large hysteresis is observed (Figure 3(d)).

After the cyclic polarization tests, the specimens were observed in the microscope. No detectable pits were observed in the specimen AR, which means that the value of 1.04  $V_{SCE}$  is more likely due to the oxygen evolution. In the other

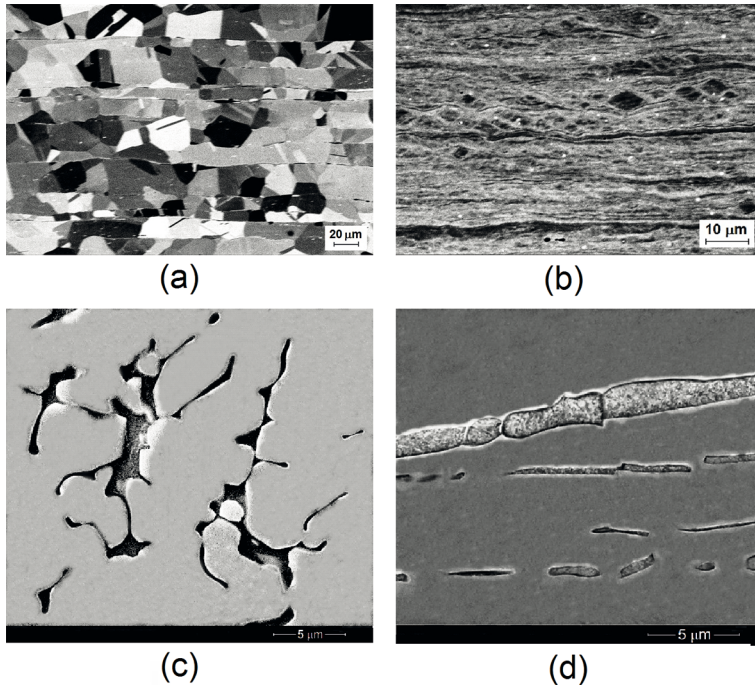


**Figure 1.** Microstructures of the AISI 317L specimens studied: (a) AR (as-received); (b) 87%-CR ( $r = 87\%$ ); (c) WM (weld metal); (d) A-450 (aged at 450°C for 400 h).

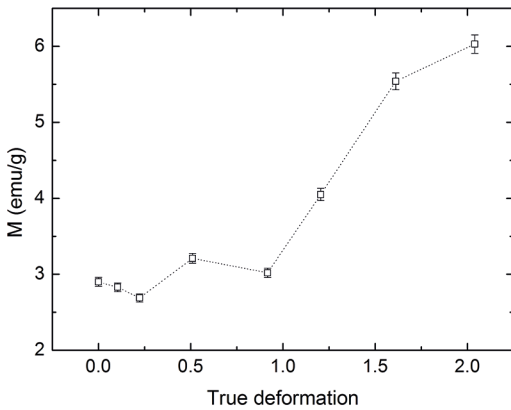


**Figure 2.** Saturation magnetization as function of true deformation.

**Table 4:** Pitting potentials ( $E_{PIT}$ ) and repassivation potentials ( $E_{RP}$ ).

Specimen	$E_{PIT}$ (V <sub>SCE</sub> )	$E_{RP}$ (V <sub>SCE</sub> )
AR (as received)	1.04 (a)	0.96
87%-CR (cold rolled 87%)	1.16	- 0.110
A-450 (aged 450°C/400h)	1.10	(b)
WM (weld metal GTAW)	0.64	(b)

Notes: (a) This value may be due to oxygen evolution, since no pits were observed after test. (b) Specimens A-450 and WM did not show repassivation, i.e. the value measured was below the open circuit potential.

specimens, however, some pits were observed in the surface after the polarization tests, as shown in Figures. 4(a-c).

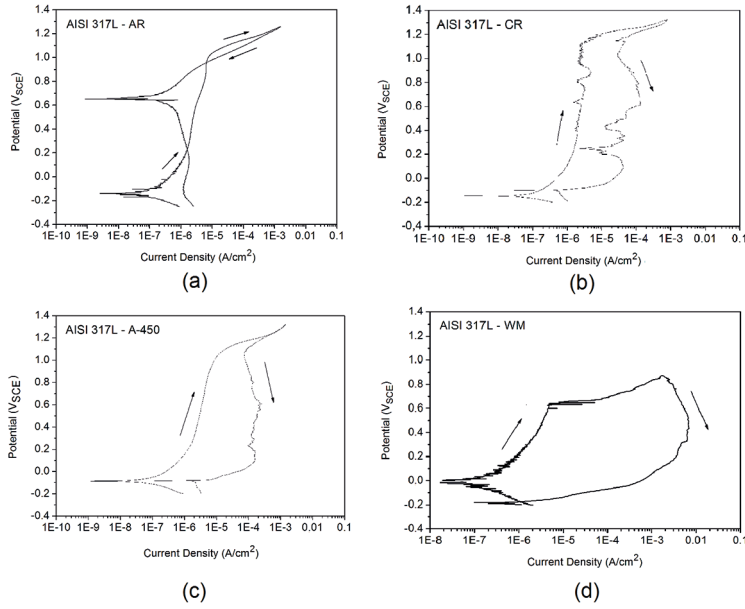
Figure 4(a) shows the pit in the cold rolled material, but it is not possible to determine if there is a preferential site for pit nucleation in the microstructure of this specimen. In specimen WM the pits nucleate in some ferrite islands where intermetallic phases have been formed, as shown in Figure 4(b). The ferrite islands are also preferential sites for pit initiation in specimen A-450 (Figure 4(c)), which is coherent with the formation of Cr-depleted  $\alpha_2$  zones due to ferrite decomposition. Since the polarization curves did not show metastable pits (Figure 3(c)), it is likely that the pits observed in the A-450 specimen had nucleated under the oxygen bubbles generated in the hydrolysis of water (crevice effect).

Table 5 shows the CPT values measured by the potentiostatic method of ASTM G-150<sup>26</sup>. The difference between 87%-CR and AR specimens is not significant, considering the standard deviation. However, WM has a CPT significantly lower than AR specimen, as shown in Figure 5, which confirms the results of cyclic polarization.

Cleland<sup>3</sup> proposed two equations to relate the CPT to the PREN:

$$CPT(^{\circ}C) = 5.0(PREN) - 104.1 \quad (6)$$

$$CPT(^{\circ}C) = 3.7(PREN) - 80.7 \quad (7)$$



**Figure 3.** Cyclic polarization curves in 3.5%NaCl (room temperature): (a) AR; (b) 87%-CR; (c) A-450; (d) WM.

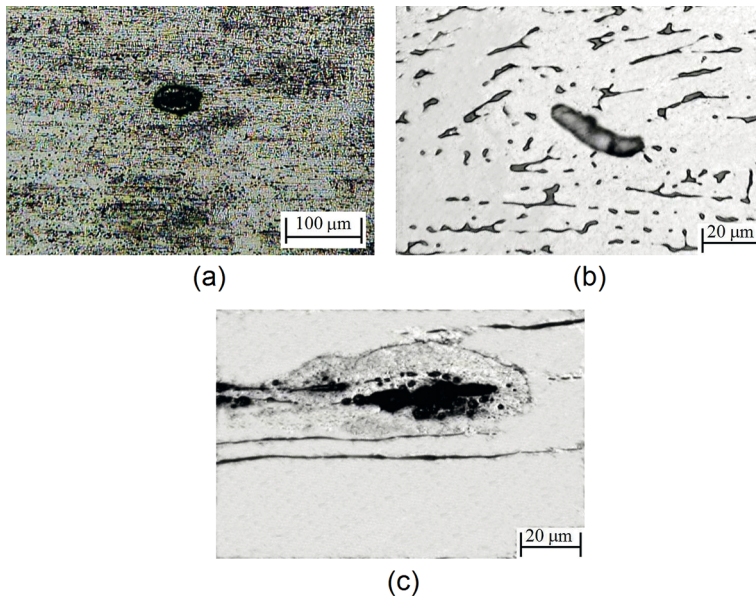


**Figure 4.** Surfaces observed after cyclic polarization tests: (a) 87%-CR; (b) WM; (c) A-450.

**Table 5:** Average CPT values.

Specimen	CPT (°C)
AR (as received)	29.0 ± 3.0
87%-CR (cold rolled 87%)	27.5 ± 4.0
A-450 (aged 450°C/400h)	see Fig. 7 and explanation
WM (weld metal GTAW)	17.5 ± 5.0

According to equations (6) and (7) the base metal has CPT values 36.4°C and 23.7°C, respectively. The value measured (29.0 ± 3.0 °C) is placed between these two estimations. In the case of WM, equations (6) and (7) give 38.6°C and 24.6°C, respectively, but the value measured (17.5 ± 5.0 °C) was lower than both predictions. This reinforces the comments of Cleland<sup>3</sup>, i.e. the CPT cannot be estimated by

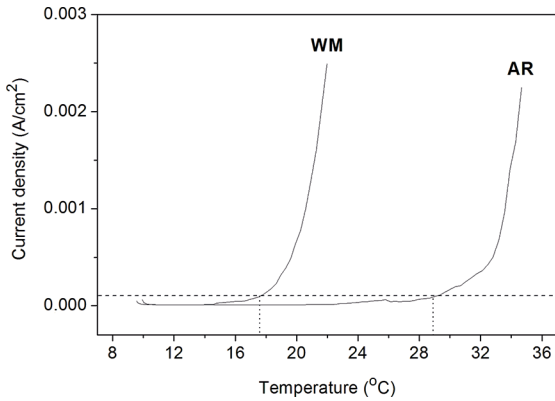


Figure 5. Curves for CPT determination in specimens WM and AR.

the PREN because many variables are not taken into account to calculate the PREN. One of these variables is, of course, the microstructure. In the WM, the precipitation of small particles of sigma phase, as shown in Figure 1(c), implies in the formation of surrounding Cr and Mo depleted areas, which is the cause of the lower CPT measured.

Figure 6 shows that when a welded joint with heat affected zone and weld metal is tested by cyclic polarization in 3.5%NaCl solution, the pitting attack was concentrated in the weld metal. Considering that PREN of HAZ and WM are very similar (see Table 2), the lower pitting resistance of the WM must be attributed to its microstructure, in accordance to the previous microstructural analysis.

Figure 7 shows the curve of current density versus temperature of specimen A-450. The behavior was different from the other specimens. Apparently, the CPT was around 34°C, which is the temperature where the current density increases abruptly. However, the current density starts above  $100\mu\text{A}/\text{cm}^2$  and remains above this value during all test. So, according to criteria of the ASTM G-150<sup>26</sup> the CPT of specimen A-450 is lower than 9°C which was the start temperature of the test. The ferrite decomposition into Cr-depleted  $\alpha_1$  and  $\alpha_2$ , even in the beginning, promotes the corrosion decay, manifested by the hysteresis in the cyclic polarization curve and the decrease of CPT.

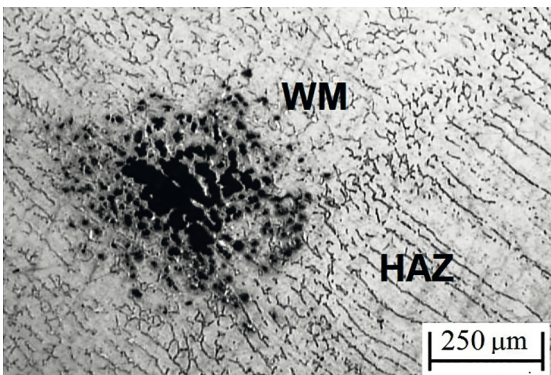


Figure 6. Preferential pitting corrosion in the weld metal after cyclic polarization test.

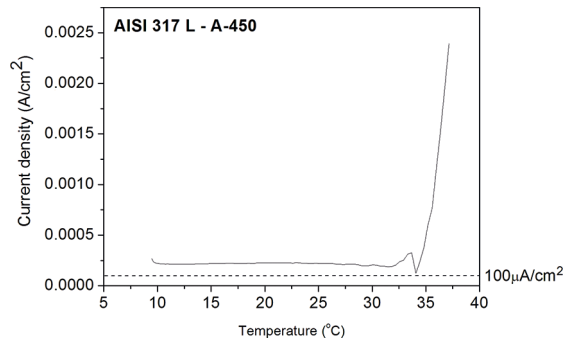


Figure 7. Curve for CPT determination in specimen A-450.

## 4. Conclusions

The investigation of the effect of microstructure on the pitting corrosion resistance of an AISI 317L stainless steel has provided the following conclusions:

- The as received solution treated material has high pitting resistance at room temperature in 3.5%NaCl solution. In fact, pits were not observed in the surface of the specimen after the cyclic polarization test, which means that the current density increase was due to oxygen evolution, and the pitting potential was high but could not be precisely determined. Besides that, the critical pitting temperature (CPT) at this heat treatment condition was  $29.0 \pm 3^\circ\text{C}$ .
- The welding by GTAW produces a dendritic microstructure of austenite and 7% of delta ferrite. Particles of  $\sigma$  phase were observed within the ferrite islands. As a consequence the pitting potential in 3.5%NaCl solution at room temperature was decreased and the CPT value was  $17.5 \pm 5^\circ\text{C}$ . In a sample including weld metal and heat affected zone there was a preferential pitting corrosion in the weld metal.
- Cold rolling with 87% of reduction creates a work hardened structure with about 2.3% of  $\alpha'$  martensite. As a consequence a decrease in the pitting resistance was detected by the hysteresis loop in the cyclic polarization curve. According to the criteria of ASTM G-150<sup>26</sup> the CPT of this specimen was lower than 9°C.
- Aging at 450°C for 400 h promotes the decomposition of delta ferrite islands. For this reason the pitting corrosion resistance decreased, as concluded by the hysteresis loop in cyclic polarization tests and the decrease of CPT.

## 5. Acknowledgements

Authors acknowledge the Brazilian Research Agencies CNPq (Grant 305294/2014-8) and FAPERJ (E-26/203033/2015) for financial support.

## 6. References

1. NACE International. *NACE 0175/ISO 15156-3: Petroleum and Natural Gas Industries - Materials For Use in H2S-Containing Environments in Oil and Gas Production - Part 3: Cracking Resistant CRAs (Corrosion Resistant Alloys) and Other Alloys*. Houston: NACE International; 2009.
2. ASM International. *ASM Specialty Handbook Stainless Steels*. Materials Park: ASM International; 1994. 576 p.
3. Cleland JH. What does the pitting resistance equivalent really tell us? *Engineering Failure Analysis*. 1996;3(1):65-69.
4. ASTM International. *ASTM A-240-16: Standard Specification for Chromium and Chromium-Nickel Stainless Steel Plate, Sheet, and Strip for Pressure Vessels and for General Applications*. West Conshohocken: ASTM International; 2016.
5. Tucker JD, Miller MK, Young GA. Assessment of thermal embrittlement in duplex stainless steel 2003 and 2205 for nuclear power applications. *Acta Materialia*. 2015;87:15-24.
6. Yao YH, Wei JF, Wang ZP. Effect of long-term thermal aging on the mechanical properties of casting duplex stainless steels. *Materials Science and Engineering: A*. 2012;551:116-121.
7. Li S, Wang Y, Wang X. Effects of ferrite content on the mechanical properties of thermal aged duplex stainless steels. *Materials Science and Engineering: A*. 2015;625:186-193.
8. Chandra K, Singhal R, Kain V, Raja VS. Low temperature embrittlement of duplex stainless steel: Correlation between mechanical and electrochemical behavior. *Materials Science and Engineering: A*. 2010;527(16-17):3904-3912.
9. Hilders O, Zambrano N. The effect of aging on impact toughness and fracture surface fractal dimension in SAF 2507 super duplex stainless steel. *Journal of Microscopy and Ultrastructure*. 2014;2(4):236-244.
10. Lo KH, Kwok CT, Chan WK, Zeng D. Corrosion resistance of duplex stainless steel subjected to long-term annealing in the spinodal decomposition temperature range. *Corrosion Science*. 2012;55:267-271.
11. May JE, de Souza CAC, Nascente PAP, Soares P, Lepienski CM, Kuri SE. Effect of thermal aging conditions on the corrosion properties and hardness of a duplex stainless steel. *Materials Research*. 2010;13(4):431-436.
12. Wang YQ, Yang B, Han J, Dong F, Wang YL. Localized Corrosion of Thermally Aged Cast Duplex Stainless Steel for Primary Coolant Pipes of Nuclear Power Plant. *Procedia Engineering*. 2012;36:88-95.
13. Eskandari M, Zarei-Hanzaki A, Mohtadi-Bonab MA, Onuki Y, Basu R, Asghari A, et al. Grain-orientation-dependent of  $\gamma$ - $\epsilon$ - $\alpha'$  transformation and twinning in a super-high-strength, high ductility austenitic Mn-steel. *Materials Science and Engineering: A*. 2016;674:514-528.
14. Hamada AS, Karjalainen LP, Misra RDK, Talonen J. Contribution of deformation mechanisms to strength and ductility in two Cr-Mn grade austenitic stainless steel. *Materials Science and Engineering: A*. 2013;559:336-344.
15. Mongonon PL, Thomas G. The martensite phases in 304 stainless steel. *Metallurgical Transactions*. 1970;1(6):1577-1586.
16. Seetharaman V, Krishnan P. Influence of the martensitic transformation on the deformation behaviour of an AISI 316 stainless steel at low temperatures. *Journal of Materials Science*. 1981;16(2):523-530.
17. Shirdel M, Mirzadeh H, Parsa MH. Nano/ultrafine grained austenitic stainless steel through the formation and reversion of deformation-induced martensite: Mechanisms, microstructures, mechanical properties, and TRIP effect. *Materials Characterization*. 2015;103:150-161.
18. Bogers AJ, Burguers WG. Partial dislocations on the {110} planes in the B.C.C. lattice and the transition of the F.C.C. into the B.C.C. lattice. *Acta Metallurgica*. 1964;12(2):255-261.
19. Reed RP, Schramm RE. Relationship between stacking fault energy and x-ray measurements of stacking fault probability and microstrain. *Journal of Applied Physics*. 1974;45(11):4705.
20. Tavares SSM, M Neto J, da Silva MR, Vasconcelos IF, de Abreu HFG. Magnetic properties and  $\alpha'$  martensite quantification in an AISI 301LN stainless steel deformed by cold rolling. *Materials Characterization*. 2008;59(7):901-904.
21. Souza Filho IR, Sandim MJR, Cohen R, Nagamine LCCM, Hoffmann J, Bolmaro RE, et al. Effects of strain-induced martensite and its reversion on the magnetic properties of AISI 201 austenitic stainless steel. *Journal of Magnetism and Magnetic Materials*. 2016;419:156-165.
22. Gauss C, Souza Filho IR, Sandim MJR, Suzuki PA, Ramirez AJ, Sandim HRZ. In situ synchrotron X-ray evaluation of strain-induced martensite in AISI 201 austenitic stainless steel during tensile testing. *Materials Science and Engineering: A*. 2016;651:507-516.
23. Tavares SSM, da Silva MR, Pardal JM, Abreu HFG, Gomes AM. Microstructural changes produced by plastic deformation in the UNS S31803 duplex stainless steel. *Journal of Materials Processing Technology*. 2006;180(1-3):318-322.
24. Tavares SSM, Pardal JM, da Silva MR, de Oliveira CAS. Martensitic transformation induced by cold deformation of lean duplex stainless steel UNS S32304. *Materials Research*. 2014;17(2):381-385.
25. ASTM International. *ASTM G61-09: Standard Test Method for Conducting Cyclic Potentiodynamic Polarization Measurements for Localized Corrosion Susceptibility of Iron-, Nickel-, or Cobalt-Based Alloys*. West Conshohocken: ASTM International; 2009.
26. ASTM International. *ASTM G150-13: Standard Test Method for Electrochemical Critical Pitting Temperature Testing of Stainless Steels*. West Conshohocken: ASTM International; 2013.
27. Lippold J, Kotecki D. *Welding Metallurgy and Weldability of Stainless Steels*. Hoboken: Wiley Interscience; 2005.